Published in final edited form as:
IEEE Trans Med Imaging. 2012 July ; 31(7): 1493–1504. doi:10.1109/TMI.2012.2194720.

Identification of Reduced-Order Thermal Therapy Models Using Thermal MR Images: Theory and Validation

Ran Niu and
Department of Chemical Engineering, University of Utah, Salt Lake City, UT 84112 USA. He is now with Real-time Controls and Instrumentation Laboratory, GE Global Research, Shanghai 201203, China

Mikhail Skliar [Senior Member IEEE]
Department of Chemical Engineering, University of Utah, Salt Lake City, UT 84112 USA

Mikhail Skliar: mikhail.skliar@utah.edu

Abstract

In this paper, we develop and validate a method to identify computationally efficient site- and patient-specific models of ultrasound thermal therapies from MR thermal images. The models of the specific absorption rate of the transduced energy and the temperature response of the therapy target are identified in the reduced basis of proper orthogonal decomposition of thermal images, acquired in response to a mild thermal test excitation. The method permits dynamic reidentification of the treatment models during the therapy by recursively utilizing newly acquired images. Such adaptation is particularly important during high-temperature therapies, which are known to substantially and rapidly change tissue properties and blood perfusion. The developed theory was validated for the case of focused ultrasound heating of a tissue phantom. The experimental and computational results indicate that the developed approach produces accurate low-dimensional treatment models despite temporal and spatial noises in MR images and slow image acquisition rate.

Index Terms

Magnetic resonance imaging (MRI); thermal therapies; tissue modeling; ultrasound specific absorption rate

I. Introduction

Thermal therapies, such as focused ultrasound surgery [1], adjuvant heating [2], [3], thermally triggered targeted drug delivery [4], and standard hyperthermia [3], are increasingly planned, optimized, and controlled with the help of treatment models. Such models describe the deposition and dissipation of thermal energy in tissues. The deposition process is usually described as specific absorption rate (SAR) by a treatment-specific means, such as ultrasound, laser, or microwave radiation, while the heat conduction and convection by blood perfusion are the primary mechanisms of heat dissipation. With the available patient- and site-specific heat deposition and dissipation models (collectively, treatment model), the optimization of the treatment plan becomes possible and may include the

Correspondence to: Ran Niu; Mikhail Skliar, mikhail.skliar@utah.edu.

Color versions of one or more of the figures in this paper are available online at http://ieeexplore.ieee.org.

selection of appropriate applicators, their spatial positioning, and the configuration of the temperature monitoring system. Model-based automatic treatment control systems can provide such advanced functionality as minimization of the treatment time without exceeding the maximum allowable temperature in the normal tissues [5], [6].

The identification of the patient-specific treatment models is a challenging task that has yet to become routine. Models based on first principals, describing physical processes of heat deposition and dissipation, depend on *a priori* unknown tissue characteristics, such as blood perfusion and SAR, which vary substantially between patients and different treatment sites. By identifying the value of these and other parameters using experimental data, accurate first-principal models may be obtained. Typically, the data are collected during pretreatment experiments that involve low-intensity subtherapeutic heating, applied to the target by the same transducer or applicators that will later be used to administer the therapy, and the measurements of the corresponding temperature response obtained with either catheterized thermal probes or noninvasively, using MRI thermometry. The standard identification techniques [7] are then used to identify patient-specific model parameters, such as perfusion and the SAR of tissues, that give the best agreement between the model predictions and the experimental data. The computer implementation of the customized first-principal models require their discretization using finite differences, elements or volumes, or other discretization methods. The result is a high-dimensional, computationally intensive model that cannot be used to perform time-sensitive tasks, such as intraoperative model-based evaluation of treatment progression [8] and automatic treatment control using model-predictive and optimizing techniques [9]–[11].

An alternative approach is to use entirely data driven, empirical modeling methods, without first postulating an appropriate first principle model for the therapy. It this case, the model structure (such as ARX or Box-Jenkins models [7]) is selected simply to capture correlation between inputs (heating) and outputs (temperature measurements) and the identified model parameters give no physical insight into the problem. The data-drive approach is especially appealing when temperature measurements are obtained using the MRI thermometry which provides noninvasively acquired detailed temperature maps anywhere in the target. Note, however, that the high dimensionality of MRI measurements (e.g., dimension of the temperature measurement vector, corresponding to 512×512 voxels of a thermal image, is 262 174 elements) may result in the identified treatment model that is equally high-dimension when the traditional identification methods are used.

In this paper, we develop a novel approach to empirical modeling of thermal therapies that produce accurate low-dimensional models based on high-dimensional MR imaging data. The starting point of the approach is the proper orthogonal decomposition (POD) of images acquired during a pretreatment experiment in order to reduce the dimensionality of the data without significant loss of information. Fundamentally, such reduction is possible because the imaging data, when viewed as an independent collection of pixels, are highly correlated in time and space. The *spatial* correlation of MR thermal image voxels reflects the dependence of temperature distribution on the specific absorption rate of the transduced energy (e.g., electromagnetic, ultrasound) and the heat dissipation by conduction and convection. *Temporal* correlation of sequential images reflects causal dependence of temperatures on the heating history and temperatures at the preceding times. We identify the basis functions of proper orthogonal decomposition to capture spatial collection in images, which then allows us to express the imaging data parsimoniously and filter out measurement noises. The temporal correlation is then captured by identifying, in the POD basis, a dynamic model relating an external heating to temperature response. Using the example of the Pennes' bioheat transfer equation [12], we then show that the identified data-driven

model can also be used to extract the information about the site-specific parameters of the first-principle models of the therapy.

The paper has the following organization. The theoretical development of the proposed approach is described in the next section. Unlike the traditional POD approach, in which the orthogonal decomposition is used to reduce the order of a *known* model, in our approach the POD is used to identify an *unknown* low-dimensional model that accurately predicts heat deposition and dissipation during thermal therapies. After describing the identification method, the theory section is concluded by establishing the relationship between the identified empirical and the postulated PDE models. The next section describes the validation results of the developed method in computer simulations and phantom experiments. The results show that the identified low-dimensional SAR and thermal response models give an accurate prediction of temperature response during noninvasive focused ultrasound (FUS) heating. The summary of the method and its discussion conclude the paper.

II. Theory

A. POD Background

The proper orthogonal decomposition is a technique often used to extract a set of basis functions for an approximate, modal-like representation of distributed parameter systems (DPS). In a typical application of the POD, a high-dimensional numerical solution of a *known* distributed parameter model is used as an input to the POD algorithm. The identi-fied reduced-order POD basis is then used with Galerkin or other projection methods to obtain a computationally efficient finite-dimensional approximation of the original infinite-dimensional DPS model. Reference [13] gives a representative example of applying this traditional approach applied to reduced-order modeling of electromagnetic phased-array tissue heating to achieve hyperthermia-range temperatures.

In this paper, the POD is used to identify an orthonormal basis of an *unknown* infinite-dimensional system based on the measurements of its dynamic response in the form of a time series of images. The fundamentals of the POD in the context of our objectives are briefly outlined as follows, with further details available in [14]–[18].

Consider a series of N images (or snapshots) U_i taken consecutively at arbitrary instants of time to characterize the evolution of a DPS defined in the spatial domain $r \in \Omega$. The problem is to obtain a function $\varphi(r)$, which is best at capturing spatial correlations in the ensemble $S = \{U_i(r): 1 \le i \le N, r \in \Omega\}$. Mathematically, the problem is to find $\varphi(r)$ such that the projections of all snapshots onto the function $\varphi(r)$ have, on average, the maximum possible value

$$\max_{\varphi, \langle \varphi, \varphi \rangle = 1} \lambda = \frac{1}{N} \sum_{i=1}^{N} \langle U_i, \varphi \rangle^2 \quad (1)$$

where $\langle f, g \rangle = \int_\Omega f(r) g(r) dr$ is the inner product of square integrable functions $f(r), g(r) \in L^2$ defined on Ω. The normalization condition $\langle \varphi, \varphi \rangle = 1$ is imposed to ensure uniqueness of the solution. If we define a correlation function

$$K(r, r') = \frac{1}{N} \sum_{i=1}^{N} U_i(r) U_i(r') \quad (2)$$

and an operator

$$R(r) \equiv \int_{\Omega} K(r, r')dr' \quad (3)$$

then the right-hand side of (1) can be expressed compactly as

$$\frac{1}{N}\sum_{i=1}^{N}\langle U_i, \varphi\rangle^2 = \int_{\Omega}\{R\varphi\}\{\varphi\}dr = \langle R\varphi, \varphi\rangle. \quad (4)$$

Comparison of (1) and (4) shows that the maximization problem (1) is equivalent to the following eigenvalue problem:

$$R\varphi = \lambda\varphi. \quad (5)$$

Therefore, the solution of (1) is the eigenfunction φ of the eigen-problem (5) corresponding to the largest eigenvalue λ. The symmetry of K implies the symmetry of R. Therefore, all eigenvalues in (5) are real and nonnegative. Assuming that all eigenvalues are ordered ($\lambda_1 \geq \lambda_2 \geq \ldots \geq \lambda_N$), the eigenfunction φ_1, corresponding to λ_1, is the desired solution of the maximization problem (1).

The general solution of the eigenproblem (5) is difficult to obtain. The problem is simplified if, following [19], we seek the solution of (5) under an additional assumption that $\varphi(r)$ can be expressed as a linear combination of snapshots

$$\varphi(r) = \sum_{i=1}^{N}\omega_i U_i(r). \quad (6)$$

With this additional assumption, (5) is written as

$$\int_{\Omega}\frac{1}{N}\sum_{i=1}^{N}U_i(r)U_i(r')\sum_{i=1}^{N}\omega_i U_i(r')dr' = \lambda\sum_{i=1}^{N}\omega_i U_i(r). \quad (7)$$

The N solutions of the eigenvalue-eigenfunction problem (7) can now be expressed as

$$\varphi_j = \sum_{i=1}^{N} w_i^j U_i(r), \quad j=1, \ldots, N \quad (8)$$

where the coefficients ω_i^j are to be determined. We introduce a covariance matrix C of all available snapshots

$$C=[c_{ij}], \quad c_{ij} = \frac{1}{N}\int_{\Omega} U_i(r)U_j(r)d\Omega, \quad i, j=1, \ldots, N. \quad (9)$$

The N solutions of (5) under the assumption (6) are given by (8), where the coefficients ω_i^j are the components of eigenvectors $W_j=[\omega_1^j \ldots \omega_N^j]^T$, $j = 1, \ldots N$, found from the following matrix eigenproblem:

$$CW_j=\lambda_j W_j. \quad (10)$$

Because C is the Hermitian matrix, eigenvectors W_j, corresponding to distinct eigenvalues, are orthogonal. The orthonormality of basis functions ($\langle \varphi_j, \varphi_j \rangle = 1$) can be enforced by the following normalization of eigenvectors:

$$\langle W_j, W_j \rangle = \sum_{i=1}^{N} \omega_i^j \omega_i^j = \frac{1}{N\lambda_j}. \quad (11)$$

The normalized eigenfunctions $\{\varphi_j\}_{j=1}^{N}=\{\varphi_1, \varphi_2, \ldots, \varphi_N\}$ form an orthonormal basis of snapshots S

$$\langle \varphi_l, \varphi_m \rangle = \begin{cases} 1, & l=m \\ 0, & l \neq m \end{cases}. \quad (12)$$

The amount of information captured by the projection of S on the ith eigenfunction is characterized by the corresponding eigenvalue λ_i. Consequently, φ_1 is the best at explaining spatial correlations in S, followed φ_2 by as the next most informative direction, and so on.

If we now define an average energy of an ensemble S as

$$E=\frac{1}{N}\sum_{i=1}^{N}\int_{\Omega} U_i(r)U_i^*(r)dr \quad (13)$$

then it is easy to show that

$$E=\sum_{j=1}^{N}\lambda_j. \quad (14)$$

Therefore, the eigenvalues can be used to guide the selection of the reduced-order POD basis, $\{\varphi_j\}_{j=1}^{M}$, $M < N$. For instance, we can select M to capture a predetermined fraction e of the total energy of the ensemble S. Specifically, we may wish to select the smallest M such that

$$\frac{\sum_{j=1}^{M}\lambda_j}{\sum_{j=1}^{N}\lambda_j} \geq e, \quad 0<e \leq 1 \quad (15)$$

where e is the value selected by a user as a tradeoff between complexity and accuracy. For higher M s the information in the ensemble $\mathcal{S}$ is captured more accurately at an expense of using a larger number of basis functions.

B. Identification of Reduced Basis From Experimental Data

Consider a set of N thermal images $T_m(r, t)$, where $r = (x, y)$ or, in the case of three-dimensional imaging, $r = (x, y, z)$. For certainty, a two-dimensional imaging is assumed;

extension to the 3-D case is trivial. Throughout the paper, all temperatures are assumed to be in the deviation form (specified as the elevation above equilibrium value), unless noted otherwise. Each image $T_m(r, t_i)$, collected at time t_i to characterize temperature distribution in the spatial domain of interest $r \in \Omega$, plays a role of a snapshot U_i. The series of N consecutive images forms an ensemble S used to identify the POD basis $\{\varphi_j\}_{j=1}^N$.

For snapshots continuously changing in Ω with r, the covariance matrix C is defined by (9). When the values of snapshots are measured in discrete locations, C must be calculated based on the pixelated values of the acquired temperature distribution. For example, in 2-D cases, the covariance coefficients

$$c_{ij} = \frac{1}{N} \int_x \int_y T_m(r, t_i) T_m(r, t_j) dx dy \quad (16)$$

may be approximated using voxel values of temperature distribution T_m according to a selected numerical integration method, such as the trapezoidal rule.

After calculating the covariance matrix according to (16), the orthonormal POD basis $\{\varphi_j\}_{j=1}^N$ is found according to the following steps: 1) First, eigenvalue problem (10) is solved to find the coefficients ω_i^j. 2) The result is then normalized according to (11). 3) Finally the basis functions $\varphi_j(r)$ are formed according to (8). In the sequel, we will assume that the identified discrete values of $\varphi_j(r)$ are arranged in a N_{vox}-dimensional vector

$$\varphi_j(r) \approx [\varphi_j(r_1)\, \varphi_j(r_2) \ldots \varphi_j(r_{N_{\text{vox}}})]^T \quad (17)$$

where r_1, r_2, … are voxel locations and N_{vox} is the total number of voxels.

Using the identified full-order basis $\{\varphi_j\}_{j=1}^N$, the *exact* representation of a given image $T_m(r, t_i)$ in S is given by the following decomposition:

$$T_m(r, t_i) = \mathcal{P}_{\varphi,N}[T_m(r, t_i)] = \sum_{j=1}^{N} \varphi_j(r) \widehat{T}_j^m(t_i). \quad (18)$$

This last expression defines the image projection operator $\mathcal{P}$ which established the relationship between thermal images $T_m(r, t_i)$ and their projections $\widehat{T}_j^m(t_i)$ onto the manifold of basis function $\varphi_j(r)$.

We can now select the reduced basis M of elements, $\{\varphi_j\}_{j=1}^M$, in order to achieve a tradeoff between the accuracy of image approximation and the complexity of the model. The subsequent validation results indicate that even for high-accuracy approximations, $M \ll N$, where M is also much smaller than the number of voxels in each image N_{vox}. This observation confirms that MR thermometry of thermal therapies produces highly correlated data.

Without a formalized criteria for the order selection, a subjective judgment in selecting M is unavoidable. In general, if M is too small, the identified model will provide an incomplete representation of the underlying process. By using a larger number of basis elements, the image data set used in model identification will be more accurately described with the

identified higher dimensional model. However, a larger than necessary number of basis elements will result in an overparameterized model which overfits the data and captures noise. Overparameterized models are also more likely to produce spurious results when compared to validation data, i.e., the data not used for model identification.

A more systematic approach requires that the model order is selected to satisfy a formal selection criterion. Equation (15) is an example of a criterion that quantifies the discussed tradeoff, with many other choices found in the literature (see, for example, [20] which discusses the order selection problem in the context of principle component analysis).

C. Thermal Model in Projection Form

In the reduced-order basis $\{\varphi_j\}_{j=1}^{M}$ of the first M elements of the full-order basis $\{\varphi_j\}_{j=1}^{N}$, the temperature distribution $T(r, t)$, inside the patient, of which an image $T_m(r, t)$ is the measurement, may be approximated as $T_p(r, t)$

$$T(r,t) \approx T_p(r,t) = \mathscr{P}_{\varphi,M}[T(r,t)] = \sum_{j=1}^{M} \varphi_j(r)\widehat{T}_j(t) = \mathbf{\Phi}(r)\widehat{T}(t) \quad (19)$$

where $\hat{T} = [\hat{T}_1(t)\ \hat{T}_2(t)\ \dots\ \hat{T}_m(t)]^T$ is the M-dimensional vector of projections of temperature distribution $T(r, t)$ into the reduced basis and $\mathcal{P}_{\phi,M}$ is the operator projecting $T(r, t)$ into the basis $\{\varphi_j\}_{j=1}^{M}$. The columns of the $N_{\text{vox}} \times M$ matrix $\mathbf{\Phi}(r) = [\varphi_1 \cdots \varphi_j \cdots \varphi_m]$ are the values of the identified eigenfunctions in all pixel locations, (17). The vector $\hat{T}(t)$ gives the complete description of the temperature distribution at time t to the specified accuracy e and defines the approximation $T_p(r, t)$ in the identified reduced-order basis.

We will assume that the same reduced basis can be used to adequately capture the shape of the power deposition $Q(r, t)$ (in W/m^3) in the tissue, which causes the temperature increase. This is a reasonable assumption because of the causal dependence of $T(r, t)$ on $Q(r, t)$. Then, similarly to (19), we obtain the approximation

$$Q(r,t) \approx Q_p(r,t) = \mathscr{P}_{\varphi,M}[Q(r,t)] = \sum_{j=1}^{M} \varphi_j(r)\widehat{u}_j(t) = \mathbf{\Phi}(r)\widehat{u}(t) \quad (20)$$

where the vector $\hat{u}(t)$ is the projection of the power deposition into the manifold defined by the reduced basis $\{\varphi_j\}_{j=1}^{M}$. With known tissue density, the specific absorption rate (in W/kg) is related to the power deposition as

$$SAR(r,t) = \frac{Q(r,t)}{\rho(r)} \approx \frac{1}{\rho(r)}\mathbf{\Phi}(r)\widehat{u}(t). \quad (21)$$

Our objective is to identify a linear continuous-time dynamic model that relates the temperature projections $\hat{T}(t)$ to the projections of the power deposition $\hat{u}(t)$

$$\dot{\widehat{T}} = A\widehat{T}(t) + B\widehat{u}(t) \quad (22)$$

where $M \times M$ matrices A and B, and M-dimensional projection vector $\hat{u}$ are unknown. Hence, the problem is to identify A, B and $\hat{u}$ such that when $\hat{T}$, predicted by (22), is used in (19), the resulting $T_p(r, t)$ gives the best possible agreement with the acquired images $T_m(r, t)$. Note that the affine term $B\hat{u}$ describes the effect of power deposition on the evolution of the projected temperatures $\hat{T}(t)$. With nonzero initial conditions and $\hat{u} = 0$, the projection model (22) describes the decay of temperature projections to thermal equilibrium $\hat{T} = 0$. Therefore, the system matrix characterizes the heat dissipation by convection and diffusion. The dissipative behavior implies that (22) must be stable (all eigenvalues of the identified must lie to the left of the imaginary axis).

The problem of identifying the treatment model in the discrete-time form was considered in [18].

D. Identification of Treatment Model in Projection Form

1) Identification of A—The power deposition pattern of a given transducer is patient- and site-specific and, therefore, *a priori* unknown. The model identification with an unknown input is an unusual problem. To decouple the problems of identifying A, B and $\hat{u}$, we first identify the system matrix based only on temperature measurements acquired during tissue cooling, with zero power input. The projection model (22) in this case takes the simplified, input-independent form

$$\dot{\hat{T}}(t) = A\hat{T}(t) \quad (23)$$

with the initial conditions $\hat{T}_0$ calculated as the least squares solution of the following equation:

$$\mathbf{\Phi}(r)\hat{T}_0 = T_m(r, t_0) \quad (24)$$

where $T_m(r, t_0)$ is the measured temperature distribution at the initial cooling time t_0. To simplify the notation, we assume that $t_0 = 0$.

We wish to identify A such that *during tissue cooling* the quadratic errors between all measured temperatures and the corresponding model predictions are minimized

$$\min_A \sum_k \|T_m(r, t_k) - T_p(r, t_k)\|_2 \quad (25)$$

where T_p is calculated from (19) using $\hat{T}(t)$ predicted by model (23).

To solve the posed problem, assume that the model predictions are perfect. Then an acquired image $T_m(r, t_k)$ must satisfy (23) and its analytical solution

$$T_m(r, t_k) = \mathbf{\Phi}(r)e^{At_k}\hat{T}_0 \quad (26)$$

where e^{At_k} is the matrix exponential. Differentiation of (26) yields

$$Ae^{At_k}\hat{T}_0 = \mathbf{\Psi}\mathbf{\Phi}^T T_t(r, t_k) \quad (27)$$

where $T_t(r, t_k)$ is the time derivative of temperature measurements and $\boldsymbol{\Psi}$ is equal to the pseudo-inverse of $\boldsymbol{\Phi}^T\boldsymbol{\Phi}$. After obvious manipulations, we arrive at the following system of linear equations, which must be solved in the least squares sense to find an unknown A:

$$T_m^T(r, t_k)\boldsymbol{\Phi}\boldsymbol{\Psi}^T A^T = T_t^T(r, t_k)\boldsymbol{\Phi}\boldsymbol{\Psi}^T. \quad (28)$$

The solution of (28) depends on a single image $T_m(r, t_k)$, which makes the identified A sensitive to temporal measurement noises. In order to obtain an accurate and robust estimation, all available images, acquired during tissue cooling, must contribute to the identification of A. We accomplish this by assembling (28), repeated for all acquired images, into the following single matrix equation:

$$\mathbf{T}_m^T\boldsymbol{\Phi}\boldsymbol{\Psi}^T A^T = \mathbf{T}_t^T\boldsymbol{\Phi}\boldsymbol{\Psi}^T \quad (29)$$

and solving it, in the least squares sense, for an unknown A. Here, $\boldsymbol{T}_m = [\,T_m(r, t_1) \cdots T_m(r, t_N)]$ and $\boldsymbol{T}_t = [\,T_t(r, t_1) \cdots T_t(r, t_N)]$ are the matrices which collect all available images and their derivatives. The derivatives must be calculated numerically, in our implementation, using the Savitsky-Golay method [21] to reduce the effect of measurement noises.

2) SAR Identification—The patient- and site-specific SAR for a given transducer is traditionally identified using the initial slope of a temperature response to the step change in transducer power [22]. With straightforward modifications, the slope method can be used to identify the power projection vector $\hat{u}$ in the projection model (22). However, an accurate estimation of the initial slope is strongly influenced by measurement noises and slow sampling rate. Therefore, our objective is to develop an alternative SAR identification method that is: 1) robust in the presence of measurement noises; 2) less affected by slow sampling rate of MRI thermometry; and 3) can be used to identify low-dimensional description of the SAR distribution. The formal problem statement is to identify the projections $\hat{u}(t)$ of $Q(r, t)$ such that the difference between *all* measured and predicted temperatures is minimized

$$\min_{B\widehat{u}} \|T_m(r, t) - T_p(r, t)\|_2 \quad (30)$$

where temperature predications T_p are given by (19) calculated using $\hat{T}$ predicted by the model (22) with the identified system matrix A. As shown in Section II-E, matrix B only depends on such tissue parameters as density ρ and heat capacity C_t, which we assume to be known in the sequel. Such an assumption is common since ρ and C_t are known for different tissue types and relatively constant with temperature. If this assumption does not hold, then only the product $B\hat{u}$ can be uniquely identified by solving the minimization problem (30).

Note that, unlike the initial slope method, it is not necessary that the power is applied as a step change. However, since the solution of the optimization problem (30) is simplified in such a case, the following assumes time invariant $Q(r)$.

Suppose that $T_m(r, t)$ is the measured temperature increase in response to a step change in the transducer power. The corresponding prediction of temperature projections $\hat{T}$ is given by the following analytical solution of (22):

$$\widehat{T}(t) = e^{At}\widehat{T}_o + (e^{At} - I)A^{-1}B\widehat{u} \quad (31)$$

where $\hat{T}_o$ is the projection of the initial temperature distribution. By rearranging (31) and multiplying it by the matrix $\mathbf{\Phi}$, we obtain that the minimal (zero) error in predicting an acquired thermal image $T_m(r, t_k)$ is obtained if $\hat{u}$ satisfies the following equation:

$$\mathbf{\Phi}(r)(e^{At_k}-I)A^{-1}B\widehat{u}+T_m(r,t_k)-\mathbf{\Phi}(r)e^{At_k}\widehat{T}_o. \quad (32)$$

Next, we assemble (32), written for all images acquired at $t_1, t_2, \ldots, t_N$ during the step test, into the following single system of equations:

$$\mathbf{\Phi}(r)\begin{bmatrix} e^{At_1}-I \\ \vdots \\ e^{At_N}-I \end{bmatrix}A^{-1}B\widehat{u}=\begin{bmatrix} T_m(r,t_1) \\ \vdots \\ T_m(r,t_N) \end{bmatrix}-\mathbf{\Phi}(r)\begin{bmatrix} e^{At_1} \\ \vdots \\ e^{At_N} \end{bmatrix}\widehat{T}_o \quad (33)$$

where the matrix pseudo-inverse should be used if A is not invertible. This last equation is simplified if the domain is initially at thermal equilibrium, which corresponds to the case of $\hat{T}_o = 0$.

The least squares solution of the assembled system of equations gives the identified power projection vector $\hat{u}$. Compared to the slope method, which estimates the SAR based only on the initial temperature response, the proposed approach utilizes all available temperature measurements, which reduces the sensitivity of the identified $\hat{u}$ to slow sampling and measurement noises. As the number of images is increased, the sensitivity of $\hat{u}$ to temporal noises is further reduced. The effect of spatial noises is reduced by using the following projection form of (33):

$$\begin{bmatrix} e^{At_1}-I \\ \vdots \\ e^{At_N}-I \end{bmatrix}A^{-1}B\widehat{u}=\begin{bmatrix} \widehat{T}_m(t_1) \\ \vdots \\ \widehat{T}_m(t_N) \end{bmatrix}-\begin{bmatrix} e^{At_1} \\ \vdots \\ e^{At_N} \end{bmatrix}\widehat{T}_o \quad (34)$$

where the vectors of measurement projections $\hat{T}_m(t_i)$, $i = 1, \ldots, N$ are found as the least square solutions of equation

$$\mathbf{\Phi}(r)\widehat{T}_m(t_i)=T_m(r,t_i)s. \quad (35)$$

The identified $\hat{u}(t)$, found by solving (33) or (34), is then used in (20) and (21) to estimate the power deposition $Q(r, t)$ and the corresponding SAR during the step test. If SAR scales linearly with the applied transducer power, as is often the case in low-intensity therapies, then the SAR for an arbitrary power is obtained by scaling the step test results.

E. Relationship Between Projection and PDE Models

The first-principle model of heat transfer in tissues is given by convection-diffusion partial differential equation, which depends on tissue vascularization, the blood flow rates, and other model parameters that are difficult to measure directly. The following Pennes' bioheat transfer equation (BHTE) [12]:

$$\rho C_t\frac{\partial T'}{\partial t}=\nabla\cdot(k\nabla T')-W_bC_b(T'-T_a)+Q \quad (36)$$

does not require detailed information on tissue vascularity or blood flow and uses an empirical blood perfusion-related parameter W_b(kg/m^{3}s) instead, which made the BHTE a

widely used heat transfer model. In (36), T' (°C) is the tissue temperature, Q(W/m^3) is the applied power distribution, ρ (kg/m^3) and k(W/m°C) are the tissue density and thermal conductivity C_t (C_b) is the specific heat of tissue in J/kg°C, and T_a is the arterial (or equilibrium) temperature.

We use the bioheat equation to demonstrate the relationship between the PDE and the identified projection models of thermal therapies. The following development, specific to Pennes' model, can be used as a guidance in establishing the connection between the projection models (22) and other types of the PDE models of thermal therapies, such as the convection-diffusion model.

The BHTE, written in terms of the deviation temperature $T = T' - T_a$, can be approximated in the reduced-order POD basis as

$$\sum_{j=1}^{M} \dot{\widehat{T}}_j(t)\varphi_j(r) = \sum_{j=1}^{M} \frac{k}{\rho C_t} \widehat{T}_j(t)\nabla^2\varphi_j(r) - \sum_{j=1}^{M} \frac{W_b C_b}{\rho C_t} \widehat{T}_j(t)\varphi_j(r) + \sum_{j=1}^{M} \frac{1}{\rho C_t} \widehat{u}_j(t)\varphi_j(r) \quad (37)$$

where we used decompositions (19) and (20) to approximate temperature and power distributions. The weak Galerkin formulation of the Pennes' model is obtained by taking the inner product of (37) with the elements $\varphi_i(r)$ of the reduced basis, yielding the following system of ordinary differential equations:

$$\dot{\widehat{T}}_i(t) = \sum_{j=1}^{M} (\langle \varphi_i(r), \alpha(r)\nabla^2\varphi_j(r)\rangle - \langle \varphi_i(r), \beta(r)\varphi_j(r)\rangle)\widehat{T}_j(t) + \sum_{j=1}^{M} \langle \varphi_i(r), \gamma(r)\varphi_j(r)\rangle \widehat{u}_j(t) \quad (38)$$

where $\alpha(r) = k/\rho C_t$, $\beta(r) = W_b C_b/\rho C_t$, $\gamma(r) = 1/\rho C_t$. The vector-matrix form of the M-dimensional projection model (38) is (22) with matrices $A = \{a_{ij}\}$, $B = \{b_{ij}\}$, where

$$a_{ij} = \langle \varphi_i(r), \alpha(r)\nabla^2\varphi_j(r)\rangle - \langle \varphi_i(r), \beta(r)\varphi_j(r)\rangle \quad (39)$$

$$b_{ij} = \langle \varphi_i(r), \gamma(r)\varphi_j(r)\rangle \quad (40)$$

and $i, j = 1, \ldots, M$. Note that with spatially invariant tissue density and heat capacity, B is a diagonal matrix $\gamma I_{M\times M}$.

Consider the case of the BHTE with known model parameters and power deposition. Then the low-dimensional projection model (22), obtained by calculating $\hat{u}$, a_{ij} and b_{ij} according to (20), (39) and (40), is the computationally efficient approximation of the fully defined Pennes' model. On the other hand, if the parameters of a PDE model are not known, they can be estimated using the projection model, directly identified from the imaging data. For example, once A is identified, (39) gives M^2 expressions from which the parameters of the BHTE can be estimated.

III. Validation

A. Computer Simulations

The 3-D inhomogeneous tissue model was used in simulations. Fig. 1 shows a 2 × 2 × 2 cm tumor in the center of the 16 × 16 × 16 cm domain. A single plane of interest (POI) $z = 0$ is used to visualize the results. The tumor is sonicated using a single focused ultrasound transducer with the following Gaussian power deposition:

$$Q(r,t)=\rho \cdot SAR(r,t) = \frac{I(t)}{\sigma_x\sigma_y\sigma_z\sqrt{(2\pi)^3}} \times \exp\left[-\frac{1}{2}\left\{\left(\frac{x-\mu_x}{\sigma_x}\right)^2+\left(\frac{y-\mu_y}{\sigma_y}\right)^2+\left(\frac{z-\mu_z}{\sigma_z}\right)^2\right\}\right] \quad (41)$$

where I (in Watts) is the applied power, and μ_r and σ_r are the mean and standard deviation of the SAR pattern in the directions $r = (x, y, z)$. The results were obtained with $\mu_r = 0$, $\sigma_r =$ 0.01m, and the maximum of Q fixed in the center of the domain $r = (0,0,0)$.

The bioheat transfer model with $\rho = 1000$ kg/m^3, $k = 0.5$ W/m°C, $C_t = C_b = 4000.0$ J/kg°C [23] was used to describe the temperature response to the applied power distribution Q. The blood perfusion-related parameter W_b was set to 0.5 kg/m^{3}s in the tumor and 1\kg/m^{3}s in the surrounding normal tissue. Both values are in the range of muscle perfusion. At the initial time $t = 0$ when the domain was in thermal equilibrium, a step increase in power from zero to $I = 4$ W was applied. The sonication continued until $t = 1350$ s when the power was switched off. The tissue cooling was modeled for $1350 < t \leq 1920$ s. The spatial approximation of the Pennes' model was obtained with $\Delta r = 0.0286$ cm in $-2 \leq r \leq 2$ and Δr = 0.30 cm in the rest of the domain for a total of ~6 million computational nodes. The temporal derivatives were approximated using $\Delta t = 1$s. The obtained computer model played the role of a virtual patient. The MRI thermometry measurements in this patient were modeled by assuming that the temperature distribution was measured every 10 s with the same spatial resolution as the numerical solution of (36). Though the developed approach can be used with images taken in multiple planes and with 3-D measurements, we assumed that thermal imaging of a single plane of interest (POI, Fig. 1) was available, mirroring the situation during MRI phantom experiments, described as follows.

A series of ~200 thermal images of the POI, 181 × 181 pixels each, collected in response to a step change in $Q(r, t)$, was used to identify empirical eigenfunctions according to the method described in Section II-B. Fig. 2 shows the first four identified eigenfunctions and the corresponding eigenvalues in descending order. Using the criterion (15), the first eigenfunction captures 99.34% of the information in all images, while $\varphi_2(r)$ captures 0.66%; the contribution of higher order basis functions is negligible.

Fig, 3(a) shows the temperature distribution in the POI at $t = 1350$ s. The shape of the temperature distribution is near Gaussian with the highest temperature rise of approximately 20°C observed in the center of the domain. Comparing the temperature distributions in Fig. 3(a) with the shape of the first basis function [Fig. 2(a)], the similarity is evident and expected φ_1 since was identified to maximize the explained spatial variation in thermal images.

Using the reduced basis $\{\varphi_j\}_{j=1}^{M}$ of either a single or two leading eigenfunctions ($M = 1$ or 2), the system matrix A was identified by solving (29). Matrix B was calculated from (40) assuming ρ and C_t are known. The projection $\hat{u}$ of the power deposition Q was identified following the method of Section II-D2. The results are summarized in Table I. The projection model (22) for $M = 1$ and 2 was then integrated using the fourth-order Runge-Kutta method to predict the evolution of $\hat{T}$. The corresponding prediction of the temperature distribution $T_p(r, t)$was calculated using (19). Fig. 3(b) and (c) shows the prediction error for the two models ($M = 1$ and 2) at $t = 1350$ s when temperatures are the highest. The maximum prediction error with a single-state model is ~0.15°C, compared to ~0.13°C error when the state vector $\hat{T}(t)$ has two components. Further examination of Fig. 3(b) and (c) shows that the two-state model predictions are clearly more accurate despite comparable maximum prediction errors.

The identified projections $\hat{u}$ were used in (20) to estimate the power deposition. The corresponding SAR was then compared with the known SAR given by (41) and plotted in Fig. 3(d). The SAR identification errors are shown in Fig. 3(e) and (f). The maximum absolute error is 64.3 W/kg with $M = 1$ (an ~25% error), compared to 10.6 W/kg (a 4.2% error) achieved when Q is identified using two basis functions ($M = 2$). The maximum error in both cases is at $r = (0, 0, 0)$ where the SAR has its peak. For both SAR models, the average identification error is substantially lower than the maximum error.

B. Experimental Validation

1) MR Thermometry and Experimental Setup—The experiments were performed with a 11 × 11 × 11 cm cubic agar phantom, prepared according to the recipe of Madsen *et al.* [24]. The power deposition field was created by a single, spherically focused, air backed ultrasound transducer with aperture diameter of 10 cm and radius of curvature of approximately 18 cm, which was operated at 1.5 MHz. The transducer was placed in the bath of degassed and deionized water inside the MR-compatible ultrasound positioning system [25]. After initial alignment, the transducer position remained fixed throughout the experiments. The transducer was driven by an amplified output of a function generator. The electrical impedance of the transducer was matched to the output impendence of the amplifier using an external LC matching circuit. The electrical power applied to the transducer was measured by a power meter.

The MR thermometry of the phantom was performed using the Siemens Trio 3T MRI scanner according to the PRF method. The water PRF shift is temperature dependent, allowing us to measure the temperature change from the phase difference of two gradient-echo images [26]. In our implementation, the temperature change ΔT_m was measured using the phase difference $\delta\varphi$ between two consecutive complex images $S_m(r, t_k)$ and $S_m(r, t_{k+1})$

$$\Delta T_m(r, t_{k+1}) = \frac{\Delta\varphi}{\alpha\gamma_g B_0 \cdot TE} \quad (42)$$

where $\alpha = -0.01$ ppm/°C is the temperature-dependent coefficient of PRF shift for aqueous tissue [27], γ_g is the gyromagnetic ratio, B_0 is the strength of the main magnetic field, and TE is the echo time; $\delta\varphi(r, t_{k+1})$ was calculated as the phase of the product $S_m(r, t_{k+1})S_m^*(r, t_k)$, where * denotes the complex conjugate operator. An improved temporal and spatial resolution of the acquired images was achieved by using a custom, receive-only surface coil, which created a localized sensitivity pattern thus minimizing interferences and improving signal-to-noise ratio. Gradient-echo sequence with the following acquisition parameters was used to obtain temperature measurements: repetition time TR = 30 ms, echo time TE = 10 ms, field-of-view FOV = 25.6 × 25.6 cm and flip angle = 25°. The voxel size of each thermal image was 2 × 2 × 3 mm. The scan time was 2.45 s with the phase resolution of 50% to increase the sampling rate. The overall image size was 128 × 64 and the k-space data were zero-filled to form a 128 × 128 data matrix of $N_{\text{vox}} = 16384$ voxels.

A representative temperature image in the transducer's coronal plane is shown in Fig. 4. The gradient scale is in °C, and the actual (rather than deviation) temperatures are shown. The phantom appears as a rectangular object above the ultrasound positioning system containing a clearly visible 45° ultrasound mirror. The region of interest (ROI) is the region of an appreciable temperature elevation. It has pixel coordinates $50 \le x \le 62$ and $20 \le y \le 60$ (a total of 13 × 41 = 533 voxels) and the physical dimension of 2.6 × 8.2 cm. As expected, the maximum temperature is observed on the line of the focal symmetry of the FUS transducer $x = 56$.

The phantom was sonicated by applying a step test from zero to either 3.5, 4.8 or 6.5 W of total electrical power. The phantom was allowed to thermally equilibrate before proceeding to the next experiment. Most of the results are shown for the case of 6.5 W of applied power, which was kept constant for the first 773 s of the experiment. The other two step-tests were used to examine the effect of the applied power on the shape of the SAR distribution; except for the applied power, they were identical to the 6.5 W step test.

A total of 499 MR thermal images, collected every 2.45 s, were acquired to characterize temperature evolution during each power step test. The images collected for $773 < t \leq 1225$ characterize tissue cooling after the power was switched off. Fig. 5(a) shows the measured temperature elevation within the ROI at $t = 773$ s when the temperature reached its peak value. The evolution of temperatures in selected locations on the line of ultrasound beam symmetry is shown in Fig. 5(b). The highest temperature increase of ~ 17.5°C was observed at $(x, y) = (56, 54)$. Location (56, 60) at the phantom-water bath interface is characterized by higher thermal losses, measurement noises, and artifacts.

2) Identification of Reduced Basis—Following the method of Section II-B, all available MR thermal images for the step test of 6.5 W were used to identify the orthonormal basis of eigenfunctions φ_j. The first four eigenfunctions in the ROI are shown in Fig, 6 with the corresponding and rapidly decaying values of λ_j. The first eigenfunction captures approximately 97.32% of the spatial correlation in the collection of 499 images, while $\varphi_2(r)$ captures only 2.46, which suggests that a sufficiently accurate approximation of thermal images can be achieved with the reduced basis $\{\varphi_j\}_{j=1}^{M}$ of one or two eigenfunctions ($M = 1$ or 2). The shape of φ_1 is similar to the shape of temperature distribution, as expected and previously seen in simulation results.

3) Identification of SAR and Thermal Response Models—Thermal images, acquired during phantom *cooling* after 773-s sonication at 6.5 W has ended, were used to identify the system matrix A of the model (22), as described in Section II-C. The results for $M = 1$ and 2 are shown in Table II. Equation (40) was used to calculate B, where the handbook values of tissue density and heat capacity ($\rho = 1000$ kg/m^3 and $C_t = 4186$ J/(kg°C) [28]) were used to calculate $\gamma(r) = 1/\rho C_t$.

After A and B were found, thermal images acquired *during* sonication were used in (33) to calculate the power projections $\hat{u}$. The obtained $\hat{u}$ was then used in (20) to identify $Q(r)$. The corresponding SAR was found from (21). The identified SAR for $M = 1$ and 2 are plotted in the scaled form in Fig. 7(a) and (b), respectively. Note a high degree of correlation between the shapes of the SAR, measured temperatures and $\varphi_1(r)$ (Fig. 7(b), Fig. 5(a), and Fig. 6(a), respectively), as expected for an unperfused phantom.

The linearity of the SAR as a function of the applied power was examined by comparing specific absorption rates identified for the step tests of 3.5, 4.8, and 6.5 W. For $M = 2$, Fig. 7(c) and (d) shows that the maximum absolute difference between the normalized SAR_1 and SAR_2, identified based on the results of 3.5 and 4.8 W step tests, and the normalized 6.5 W SAR_3 of Fig. 7(b) is 18.18 kg^{-1}(3.12%) and 17.89 kg^{-1} (2.18%), respectively. Such close agreement indicates that in our experiments, the SAR changed linearly with the applied power.

The prediction accuracy of the identified models (Table II) was investigated next. First, the model-predicted $\hat{T}$ was compared with the projections $\hat{T}_m(t_i)$, obtained by solving (37) for each acquired image $T_m(r, t_i)$. Fig. 8 shows an excellent agreement between $\hat{T}_m$ and $\hat{T}$ (dashed line) predicted by the two-state model. The plot of $\hat{T}_1(t)$ is similar in shape to the temperature increase in fixed spatial positions [cf., Fig. 5(b)], which indicates that the first

state of the projection model captures most of the slow temporal changes in the series of thermal images. The largest predication errors are observed during rapid changes in the applied power at $t = 0$ and $t = 773$ s when the transducer is switched on and off.

The projections $\hat{T}(t)$ predicted by the identified model (22) were then used in (19) to reconstruct the temperature distribution $T(r, t)$ in the ROI. In essence, these projections describe temporal evolution of the coefficients in the following decomposition of the temperature distribution $T(r, t)$ in the identified basis: $\{\varphi_j(r)\}_{j=1}^{M}$:

$$T(r,t)=\sum_{j=1}^{M}\varphi_j(r)\widehat{T}_j(t). \quad (43)$$

Using experimental results for comparison, the accuracy of thus predicted temperature distribution $T(r, t)$ was characterized as a function of time and space. The evolution of the spatial mean and standard deviation (STD) of prediction errors was calculated by taking an expectation over all pixels in the ROI at each image acquisition time. The result, shown in Fig. 9(a) and (b), indicates a smaller mean error and STD achieved with the two-state model. The errors are the largest following rapid changes in input power, and the two-dimensional model is better at capturing these fast transitions. Fig. 9(c) and (d) depicts the time-averaged prediction error in each pixel within ROI for $M = 1$ and 2 models. The corresponding standard deviation is shown in Fig. 9(e) and (f). Predictions of both models agree well with the measurements, though the two-state model is clearly more accurate. Note consistently larger prediction errors at the interface $y = 60$ where the PRF-water-shift temperature measurements are affected by a large water volume in the bath.

The history of predicted and measured temperatures in two voxels on the line of ultrasound beam symmetry is shown in Fig. 10(a) and (b). Fig. 10(c) and (d) shows the snapshots of predicted and measured temperatures on the line $x = 56$ at two different instants. The examination of Fig. 10 shows that prediction errors are larger after rapid temporal SAR changes and reduce gradually as temperature tends to a steady state value. The single-state model gives reasonably good predictions, while the predictions of the two-state model agree with measurements very closely.

IV. Discussion

The methods for the identification of low-dimensional models of thermal therapies based on MR thermometry imaging were developed and validated. The method consists of the following steps.

1. The identification procedure starts with pretreatment experiments to collect patient- and site specific MR thermal images, $U_i(r)$, $i=\overline{1, N}$, characterizing the response of the target, the surrounding, and the intervening normal tissues to low, subtherapeutic level of heating. The images should also be acquired during tissue cooling back to normal value, after an external heating has been stopped.
2. The images collected during the pretreatment experiment must be used to obtain the reduced-order basis for a parsimonious description of the specific absorption rate and the temperature distribution inside the patient. To find the reduced basis $\{\varphi_j\}_{j=1}^{M}$:
    1. eigenvalue problem (10) is solved first;

2. obtained eigenvectors W_j are normalized according to (11) to ensure orthonormality of the basis;
3. elements of the normalized eigenvector are then used as coefficients in the decomposition (8) to obtain the basis functions φ_j;
4. number of the basis functions M is selected to satisfy condition (15) or some other appropriately selected criterion.

3. The reduced basis is then used to identify the specific ab-sorbtion rate of the applied energy and a low-dimensional, dynamic projection model, which gives computationally efficient predictions of the patient's thermal response to external heating.
    1. Using only images acquired during tissue cooling, the system matrix A is identified as a least squares solution of the linear matrix (29).
    2. The power deposition in the projected form $\hat{u}(t)$ is identified based on images acquired during active heating of tissues, by finding the least square solution of the linear system of (34), or (33). Using the result in (20) and (21) gives the estimate of the power deposition, $Q(r, t)$, and the corresponding SAR for the transducer used to heat the tissues. The matrix B of the reduced order model is given by (40).

Thus, identified thermal model (22) predicts evolution of temperature projections $\hat{T}(t)$, from which the temperature distribution $T(r, t)$ is obtained using decomposition (19).

The described identification procedure is data driven and independent of the assumptions on the underlying partial differential equations governing the heat transfer in tissues. As a result, after the model (22) is obtained, it can be used to estimate the parameters of the assumed governing model, such as the blood perfusion coefficient of the bioheat equation.

The identification results obtained following the developed approach are less sensitive to temporal and spatial measurement noises in acquired images, and slow image acquisition rate. No prior knowledge is required to identify the thermal response model. However, independent information on tissue density and heat capacity (which define matrix B) is required to identify the power deposition and the corresponding SAR.

Computer simulations of focused ultrasound heating of a tumor were used to demonstrate the ability of the developed method to identify accurate treatment models of low dimensionality. It was found that the SAR and evolving temperature distribution in a very large number of computational nodes can be accurately represented by the identified projection model with only two states and that the accuracy of the low-dimensional approximation can be controlled by selecting the number of basis elements.

The developed approach was further tested in MRI experiments. The results confirm that the low-dimensional thermal response model, identified from a sequence of MRI thermal images, accurately describes temperature response of a tissue phantom to focused ultrasound heating. The true SAR during the experiments was not known and thus unavailable for direct comparison. However, when the identified SAR was used to predict the temperature distribution, the agreement with measurements was very good. This observation together with the consistency of the identified SAR in multiple tests provide an experimental validation of the developed SAR identification method. Note that the SAR can only be identified if density and heat capacity of tissues are known. If $\rho(r, t)$ and $C_t(r, t)$ are not known, then only the product $B\hat{u}$ can be identified, which is sufficient to predict the temperature response to ultrasound heating, but not the unique SAR.

The most computationally intensive part of the method is the solution of a high-dimensional eigenvalue problem (10). This solution is carried out offline. Therefore, the basis $\{\varphi_j\}_{j=1}^{M}$ and the treatment model, identified prior to the actual thermal therapy, do not account for the changes in tissue and SAR properties during the treatment. To better capture changing tissue and SAR properties it is advisable to select a larger number of eigenfunctions M than suggested by offline analysis. Furthermore, the described method can be used without modifications to adaptively reidentify the model (22) using images acquired in real time, during the therapy. Such model adaptation will improve the ability to adequately capture the effects tissue nonlinearities at high treatment temperatures needed for ablation.

The quality of the model will also be improved if the basis $\{\varphi_j\}_{j=1}^{M}$ is also dynamically reidentified. However, this requires a rapid solution of a high-dimensional eigenvalue problem, which should be possible when recursive methods, such as those described in [29], [30], are used.

The developed approach is not limited to focused ultrasound therapies; it can be broadly used to identify a low-dimensional model of noninvasive or invasive therapies based on acquired thermal images. After straightforward modifications, the approach can be used with images acquired in multiple planes and with 3-D measurements.

Acknowledgments

The authors would like to thank Dr. C. Chen for help with 3-D simulations, and T. Perry, D. Cooley and Dr. J. Guo (all with the University of Utah) for help in conducting phantom experiments.

References

1. Kennedy JE. High-intensity focused ultrasound in the treatment of solid tumours. Nature Rev Cancer. 2005; 5:321–327. [PubMed: 15776004]
2. van der Zee J, Gonzalez D, van Rhoon G, van Dijk J, van Putten W, Hart A. Comparison of radiotherapy alone with radiotherapy plus hyperthermia in locally advanced pelvic tumours: A prospective, randomised, multicentre trial. Lancet. 2000; 355:1119–1125. [PubMed: 10791373]
3. Wust P, Hildebrandt B, Sreenivasa G, Rau B, Gellermann J, Riess H, Felix R, Schlag P. Hyperthermia in combined treatment of cancer. Lancet Oncol. 2002; 3:487–497. [PubMed: 12147435]
4. MacEwan SR, Callahan DJ, Chilkoti A. Stimulus-responsive macromolecules and nanoparticles for cancer drug delivery. Nanomedicine. 2010; 5:793–806. [PubMed: 20662649]
5. Arora D, Skliar M, Roemer R. Model-predictive control of hyperthermia treatments. IEEE Trans Biomed Eng. Mar; 2002 49(3):629–639. [PubMed: 12083297]
6. Arora D, Skliar M, Roemer R. Minimum-time thermal dose control of thermal therapies. IEEE Trans Biomed Eng. Jan; 2005 52(1):191–200. [PubMed: 15709656]
7. Ljung, L. System Identification Theory for the User. 2. Engle-wood Cliffs, NJ: Prentice—Hall PTR; 1999.
8. Jolesz FA. Future perspectives for intraoperative MRI. Neurosurg Clin N Amer. 2005; 16:201–213. [PubMed: 15561539]
9. Arora D, Skliar M, Cooley D, Roemer R. Constrained predictive control of thermal therapies for minimum time delivery of thermal dose. IEEE Trans Contr Syst Technol. Aug; 2007 15(8):1030–1037.
10. Niu R, Blankespoor A, Moellmer J, Roemer R, Skliar M. Automatic control of focal trajectory and intensity of ultrasound phased array for thermal dose delivery with normal tissue constraints: A computationally efficient method with MR-Thermometry feedback. Am Inst Phys. 2007:68.
11. Niu, R.; Skliar, M. Constrained dynamic control of focal trajectory and intensity of phased array ultrasound thermal therapies. presented at the Amer. Control Conf; San Fransisco, CA. 2011.

12. Pennes H. Analysis of tissue and arterial blood temperatures in resting human forearm. J Appl Physiol. 1948; 1:93–122. [PubMed: 18887578]
13. Kowalski ME, Jin J. Model-order reduction of nonlinear models of electromagnetic phased-array hyperthermia. IEEE Trans Biomed Eng. Jul; 2003 50(7):1243–1254. [PubMed: 14619994]
14. Holmes, P.; Lumley, J.; Berkooz, G. Turbulence, Coherent Structures, Dynamical Systems and Symmetry. Cambridge, U.K: Cambridge Univ. Press; 1996.
15. Park H, Cho D. The use of the Karhunen-Loeve decomposition for the modeling of distributed parameter systems. Chem Eng Sci. 1996; 51:81–98.
16. Sirovich, L. New Perspectives in Turbulence. New York: Springer-Verlag; 1991.
17. Ravindran S. A reduced-order approach for optimal control of fluids using proper orthogonal decomposition. Int J Numerical Methods Fluids. 2000; 34:425–448.
18. Niu R, Skliar M. Identification of controlled-complexity thermal therapy models derived from magnetic resonance thermometry images. PLoS ONE. 2011:6e26830.10.1371/journal.pone.0026830
19. Sirovich L. Turbulence and the dynamics of coherent structures: Parts i–iii. Q Appl Math. 1987; 45:561–590.
20. Valle S, Li W, Qin SJ. Selection of the number of principal components: The variance of the reconstruction error criterion with a comparison to other methods. Indust Eng Chem Res. 1999; 38(11):4389–4401.
21. Mitra, S.; Kaiser, J. Handbook for Digital Signal Processing. New York: Wiley-Interscience; 1993.
22. Roemer R, Fletcher A, Cetas T. Obtaining local SAR and blood perfusion data from temperature measurements: Steady state and transient techniques compared. Int J Radiat Oncol Biol Phys. 1985; 11:1539–1550. [PubMed: 4019278]
23. Duck, FA. Physical Properties of Tissue: A Comprehensive Reference Book. London, U.K: Academic; 1990.
24. Madsen E, Frank G, Dong F. Liquid or solid ultrasonically tissue-mimicking materials with very low scatter. Ultrasound Med Biol. 1999; 24:535. [PubMed: 9651963]
25. Arora D, Cooley D, Perry T, Skliar M, Roemer R. Direct thermal dose control of constrained focused ultrasound treatments: Phantom and in-vivo evaluation. Phys Med Biol. 2005; 50:1919–1935. [PubMed: 15815104]
26. Ishihara Y, Calderon A, Watanabe H, Okamoto K, Suzuki Y, Kuroda K, Suzuki Y. A precise and fast temperature mapping using water proton chemical shift. Magn Reson Med. 1995; 34:814–823. [PubMed: 8598808]
27. Peters R, Hinks R, Henkelman R. Ex vivo tissue-type independence in proton-resonance frequency shift MR thermometry. Magn Reson Med. 1998; 40:454–459. [PubMed: 9727949]
28. Chato, JC.; Lee, RC. The future of biothermal engineering. In: Diller, RK., editor. Biotransport: Heat and Mass Transfer in Living Systems. Vol. 858. New York: Ann. NY Acad. Sci; 1998. p. 1-20.
29. Yu K. Recursive updating the eigenvalue decomposition of a covariance matrix. IEEE Trans Signal Process. Jul; 1991 39(7):1136–1145.
30. Ding M, Tian Z, Xu H. Adaptive kernel principal component analysis. Signal Process. 2010; 90:1542–1553.

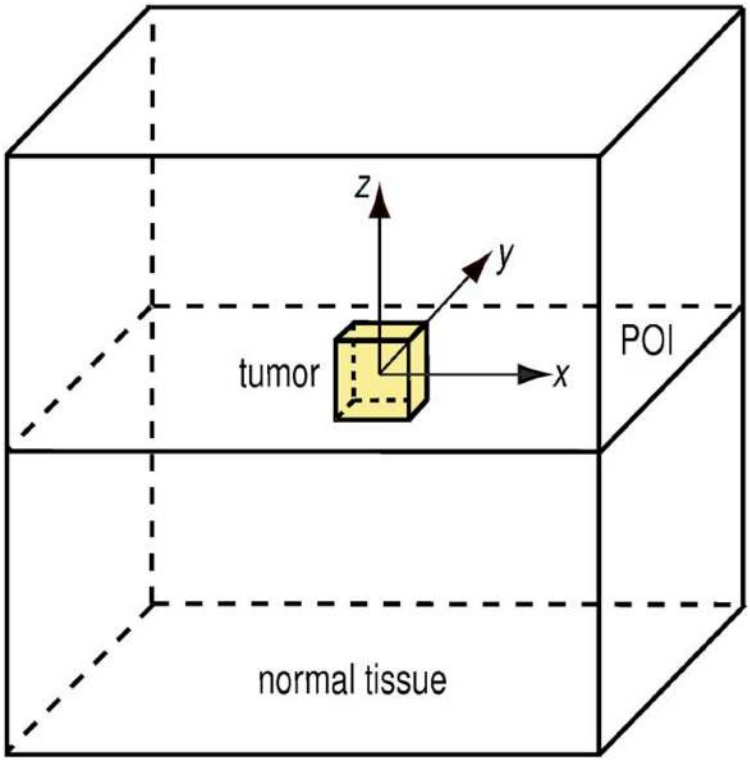

Fig. 1.
Simulated target of FUS heating.

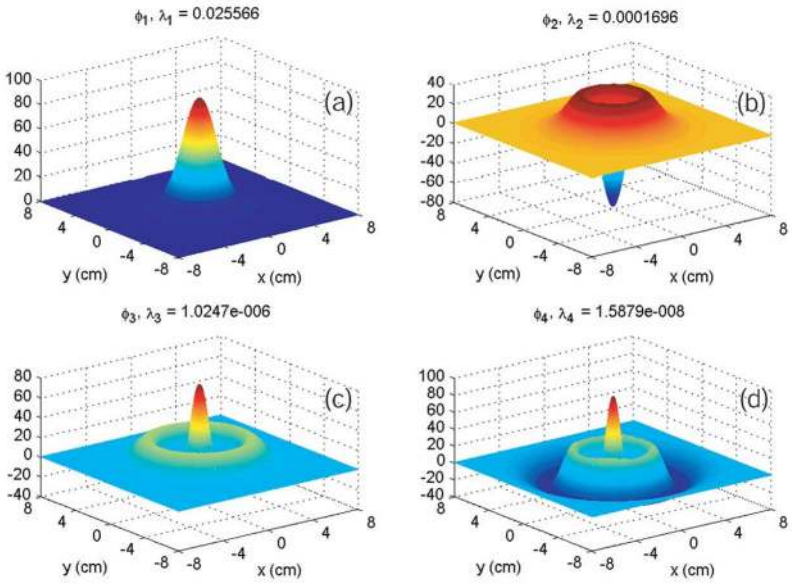

Fig. 2.
Identified basis functions and corresponding eigenvalues.

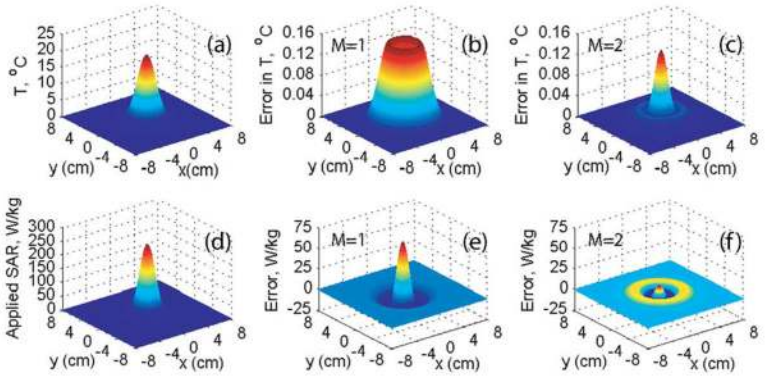

Fig. 3.

(a) Temperature measurements in POI at $t = 1350$ s. (b), (c) Temperature prediction errors of single- and two-state projection models at $t = 1350$ s. (d) SAR distribution in POI. (e), (f) SAR identification errors at $t = 1350$ s using reduced basis $\{\varphi_j\}_{j=1}^{M}$ with $M = 1$ and 2.

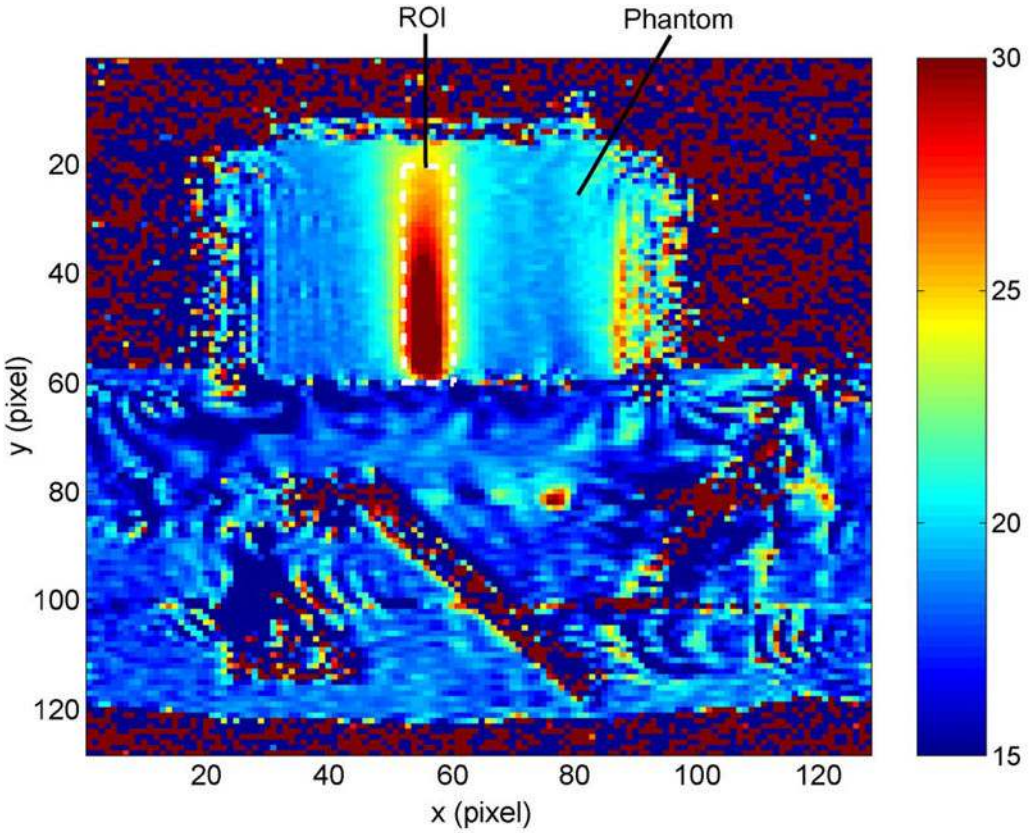

Fig. 4.
Thermal image of agar phantom, acquired at $t = 7736$ s.

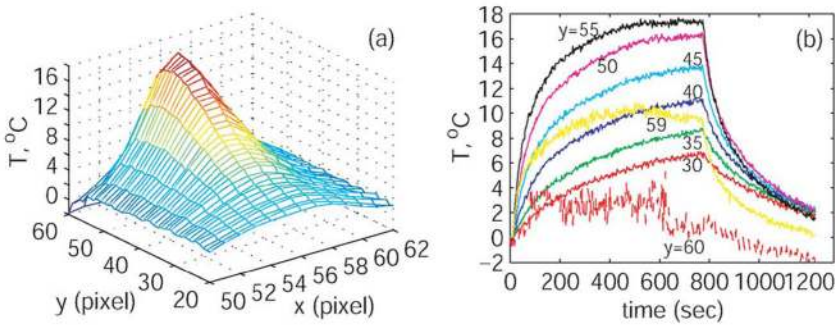

Fig. 5.

(a) MRI measurements of temperature increase in ROI at $t = 773$ s. (b) MR-measured temperature increase on line $x = 56$.

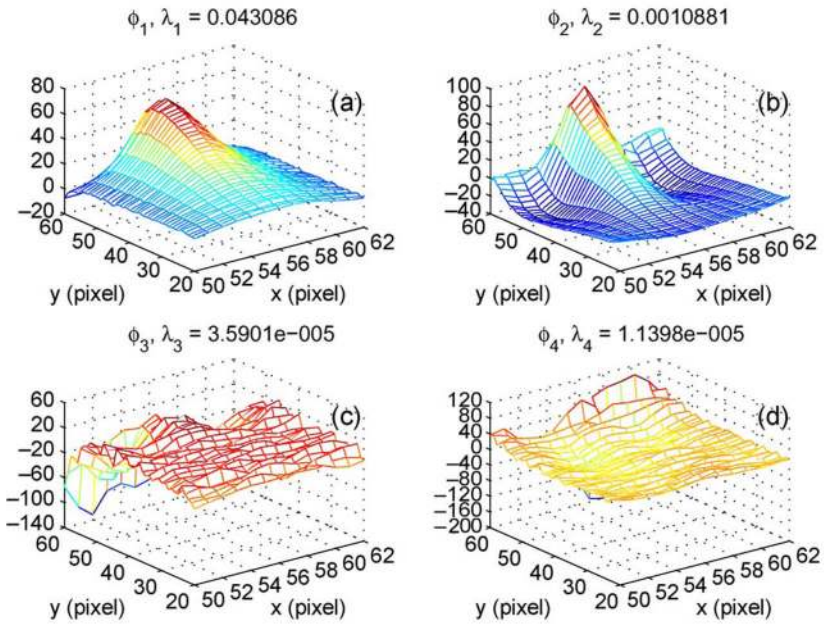

Fig. 6.
Identified eigenfunctions.

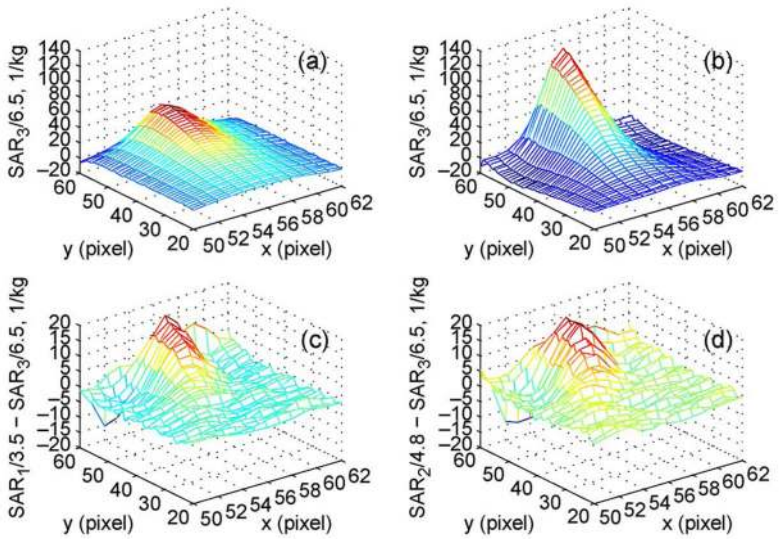

Fig. 7.

(a), (b) Identified SAR in scaled form for 6.5 W of applied power; results for $M = 1$ and $M = 2$, respectively. (c), (d) Relative difference in normalized SARs (in 1/kg) identified for different applied powers and $M = 2$. Each distribution is scaled with the corresponding total applied power of 3.5, 4.8, or 6.5 W.

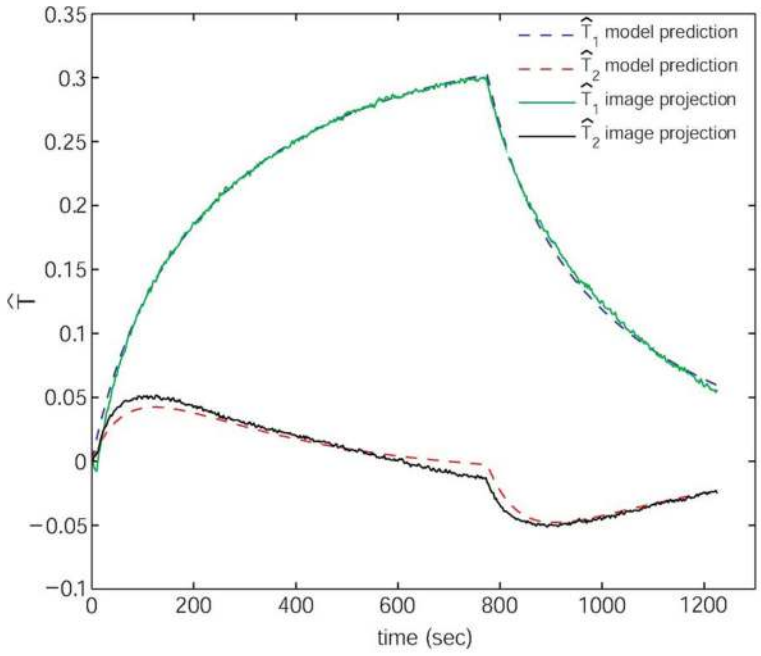

Fig. 8.
Comparison of model-predicted temperature projections, $\hat{T}(t)$, with projections of MRI thermal images $\hat{T}_m(t)$.

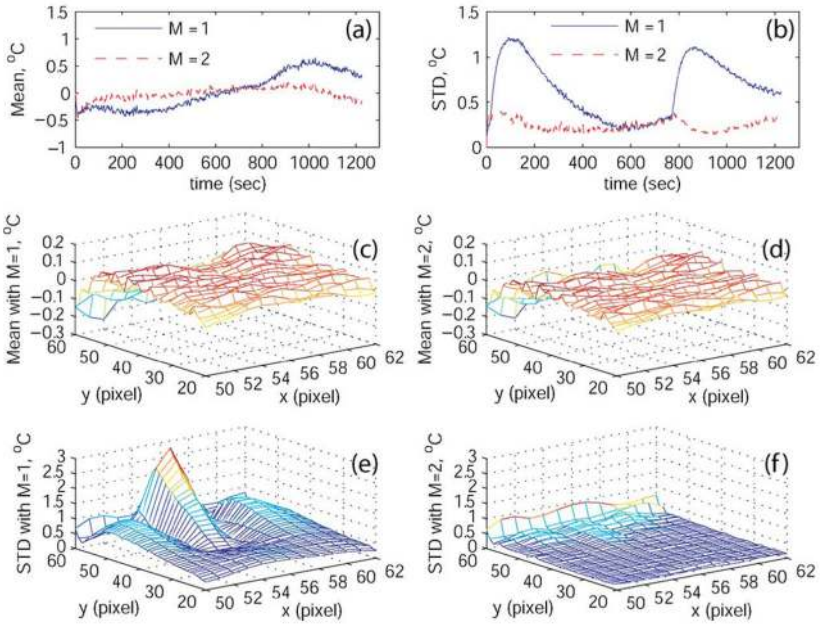

Fig. 9.

(a), (b) Spatial mean and standard deviation of prediction errors in the ROI. (c), (d) Temporal mean of prediction errors with $M = 1$ and 2. (e), (f) Temporal standard deviation of prediction errors.

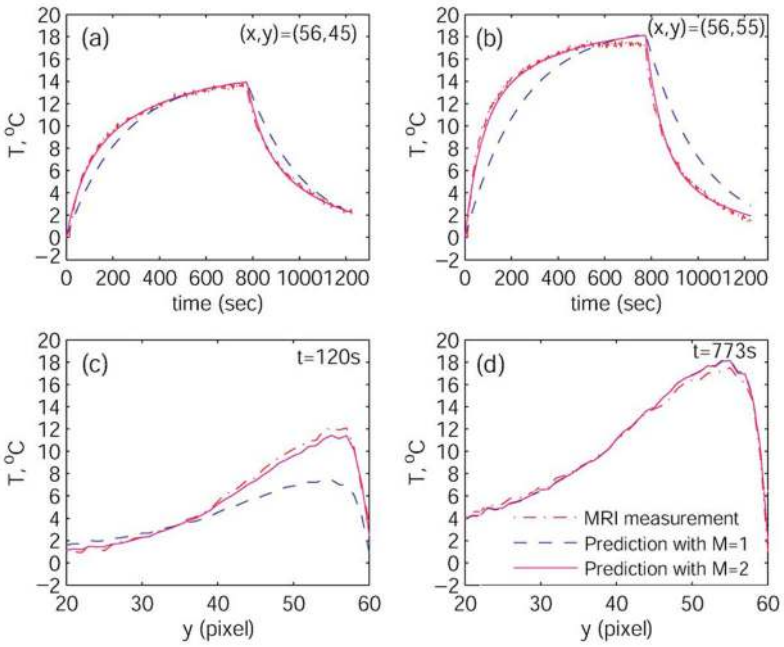

Fig. 10.

(a), (b) Evolution of temperature elevations in two selected voxels. (c), (d) Spatial distribution of temperatures on the line of focal symmetry at two different times.

TABLE I

Validation Based on Computer Simulations: Identified Thermal Response Models and Sar Projections for Reduced Basis $\{\varphi_j\}_{j=1}^{M}$

	$M = 1$	$M = 2$
A	−0.0021	$\begin{bmatrix} -0.0019 & 0.0004 \\ 0.0009 & -0.0037 \end{bmatrix}$
B	2.50×10^{-7}	$\begin{bmatrix} 0.250 & 0.0 \\ 0.0 & 0.250 \end{bmatrix} \times 10^{-6}$
$\hat{u}$	213.7323	$\begin{bmatrix} 202.7532 \\ -78.1155 \end{bmatrix}$

TABLE II

Experimental Validation: Identified Thermal Response Models and Sar Projections for Reduced Basis $\{\varphi_j\}_{j=1}^{M}$

	$M = 1$	$M = 2$
A	-0.0041	$\begin{bmatrix} -0.0060 & -0.0077 \\ -0.0035 & -0.0118 \end{bmatrix}$
B	$\gamma = 2.389 \times 10^{-7}$	$\gamma I_{2\times 2}$
$\hat{u}$	5.4310×10^{3}	$\begin{bmatrix} 7.8439 \\ 4.1554 \end{bmatrix} \times 10^{3}$